J. Fluid Mech. (2021), *vol*. 916, R2, doi:10.1017/jfm.2021.217

Receptivity and stability of hypersonic leading-edge sweep flows around a blunt body

Youcheng Xi[1], **Jie Ren**[2], **Liang Wang**[1] **and Song Fu**[1],†

[1]School of Aerospace Engineering, Tsinghua University, Beijing 100084, PR China

[2]Department of Mechanical Engineering, Faculty of Engineering, University of Nottingham, Nottingham NG7 2RD, UK

(Received 30 September 2020; revised 17 January 2021; accepted 10 March 2021)

This study performs global stability/receptivity analyses of hypersonic flows over a swept blunt body with infinite span. For the first time, we obtain the characteristics of the leading attachment-line mode to the variation of sweep angles from 20° to 70°. The global eigenfunctions exhibit the characteristics of the attachment-line instability at the leading edge. At the same time, cross-flow (at small sweep angles) or second Mack mode (at larger sweep angles) dominates further downstream. We establish an adjoint-based bi-orthogonal eigenfunction system to address the receptivity problem of such flows to any external forces and boundary perturbations. The receptivity analyses indicate that the global modes are the most responsive to external forces and surface perturbations applied in the vicinity of the attachment line, regardless of the sweep angles. It is also proven that the present global extension of the bi-orthogonal eigenfunction system can be successfully applied to complex hypersonic flows.

Key words: boundary layer receptivity, boundary layer stability, compressible boundary layers

1. Introduction

The studies of three-dimensional sweep boundary layers date back to years ago. Most of them are based on local models: the attachment-line models and three-dimensional cross-flow models. The sweep flow at the leading edge is often modelled by the sweep Hiemenz configuration, and the most unstable mode is symmetric along the chordwise direction perpendicular to the attachment line (Lin & Malik 1996; Theofilis 1998; Obrist & Schmid 2003). Further downstream, because of the non-alignment in three-dimensional inviscid streamlines and pressure gradients, an inflection point appears in the velocity profile of the three-dimensional boundary layer which leads to cross-flow instability (Reed & Saric 1989; Saric, Reed & White 2003). Two types of cross-flow instability have been

† Email address for correspondence: fs-dem@tsinghua.edu.cn

identified: travelling and stationary modes. The stationary mode plays an important role in the roughness-induced transition while travelling modes are related to external and unsteady perturbations. The dominance of either type of mode depends on the specific configurations and the disturbance environment.

The global stability analyses (GSA) around a swept parabolic body in hypersonic flows were performed by Mack, Schmid & Sesterhenn (2008) and Mack & Schmid (2011). They were able to uncover a global spectrum containing boundary-layer modes, acoustic modes and wave-packet modes. For the first time, these authors not only addressed the attachment-line instabilities, but also showed the connection of attachment-line modes with cross-flow instability through GSA, though Bertolotti (1999) had furnished strong evidence for such connection in local stability analysis. Recently, Meneghello, Schmid & Huerre (2015) performed global stability, receptivity and sensitivity analyses for incompressible flows around a Joukowski airfoil. They found that the global eigenfunction was the most responsive to forces applied in the vicinity of the attachment line. However, the analyses of such flows in the hypersonic region are quite limited.

The receptivity process describes the procedures of penetration of external perturbations into the boundary layer and excitation of modes inside the boundary layer, which plays an important role in the boundary-layer transition. Based on theoretical methods, such as finite-Reynolds-number methods (Choudhari 1994) and triple-deck theory (Ruban 1984), the bi-orthogonal eigenfunction system was found to be an effective tool for the local receptivity analyses (Hill 1995; Fedorov & Khokhlov 2002; Tumin 2007). Recently, a comprehensive review of this method is given by Tumin (2020). However, there exists no application of this approach to complex hypersonic flows.

There are two objectives in the present work. Firstly, it is to understand the stability features of hypersonic attachment-line instability over a large range of sweep angles. Secondly, it is to highlight the receptivity behaviours in the vicinity of the leading edge of a swept blunt body in hypersonic flows with the multi-dimensional bi-orthogonal eigenfunction system. This paper is organized as follows. In § 2, the governing equations are introduced and the bi-orthogonal eigenfunction system for the global stability system is established for solving the receptivity problem. The results for global stability/receptivity analysis are presented in § 3 and the conclusion is given in § 4.

2. Theoretical framework

The stability analyses of hypersonic steady flows is performed around the front part of a blunt body, as sketched in figure 1. In general, the compressible Navier–Stokes equations for variable $\boldsymbol{Q} = (\rho, u, v, w, T)$, denoting the density, velocity components and temperature, can be written as

$$\boldsymbol{\Gamma}\frac{\partial \boldsymbol{Q}}{\partial t} = \mathscr{R}(\boldsymbol{Q}), \tag{2.1}$$

where $\boldsymbol{\Gamma}$ is the coefficient matrix between conservative and primitive variables. The linearized Navier–Stokes equations (LNSE) around a stationary state $\boldsymbol{Q}$, with $\mathscr{R}(\boldsymbol{Q}) = 0$, can be represented by the combination of a linearized operator $\mathscr{L} = \partial\mathscr{R}/\partial\boldsymbol{Q}$ and a perturbation $\boldsymbol{p} = (\hat{\rho}, \hat{u}, \hat{v}, \hat{w}, \hat{T})$ field. This process forms a homogeneous system as

$$\boldsymbol{\Gamma}\frac{\partial \boldsymbol{p}}{\partial t} - \mathscr{L}\boldsymbol{p} = 0. \tag{2.2}$$

The solution of the above problem (2.2) is obtained with the method of Laplace transform.

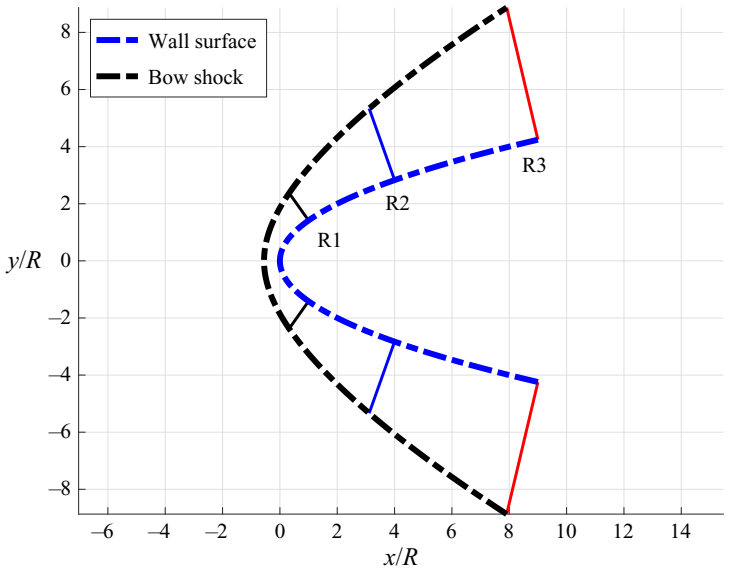

Figure 1. Outline of the computational domains of swept parabolic body ($x = y^2/2R$). Here R represents the radius of the leading edge. Three domains, bounded by the wall surface, bow shock and solid lines, which are marked by R1, R2 and R3 from the smallest to the largest, are used for calculation of direct/adjoint eigenvalue problems.

The Laplace transform $\hat{\boldsymbol{p}}(\sigma)$ of function $\boldsymbol{p}(t)$ in (2.2) is calculated from the following integral

$$\hat{\boldsymbol{p}}(\sigma) = \int_0^\infty \boldsymbol{p}(t)\,\mathrm{e}^{-\sigma t}\,\mathrm{d}t, \tag{2.3}$$

with σ being a complex parameter and $\sigma = -\mathrm{i}\omega$. From $\hat{\boldsymbol{p}}(\sigma)$, the original function $\boldsymbol{p}(t)$ can be restored with the Bromwich integral:

$$\boldsymbol{p}(t) = \frac{1}{2\pi\mathrm{i}} \oint_{-\infty-\mathrm{i}\infty}^{\infty+\mathrm{i}\infty} \hat{\boldsymbol{p}}(\sigma)\,\mathrm{e}^{\sigma t}\,\mathrm{d}\sigma = -\frac{1}{2\pi} \oint_{-\infty-\mathrm{i}\infty}^{\infty+\mathrm{i}\infty} \hat{\boldsymbol{p}}(\omega)\,\mathrm{e}^{-\mathrm{i}\omega t}\,\mathrm{d}\omega. \tag{2.4}$$

The inversion integral (2.4) suggests that the solution of LNSE (2.2) can be represented as the superposition of normal modes, which can be written as

$$\boldsymbol{p} = \hat{\boldsymbol{p}}\,\mathrm{e}^{-\mathrm{i}\omega t} + \text{c.c.} \tag{2.5}$$

where c.c. is the complex conjugate. Substitution of (2.5) into (2.2) leads to a standard global stability problem (Theofilis 2011):

$$(-\mathrm{i}\omega\boldsymbol{\Gamma} - \mathscr{L})\,\hat{\boldsymbol{p}} = 0. \tag{2.6}$$

The detailed expressions of these operators were given in the authors' previous work (Xi, Ren & Fu 2021).

On the wall surface and the bow shock, all perturbations except for the density are set to zero ($(\hat{u},\ \hat{v},\ \hat{w},\ \hat{T}) = 0$). Along the chordwise direction, at the exits, high-order extrapolations are applied for all perturbations. Because the operators are non-self-adjoint and the eigenfunctions are not orthogonal, a complete solution of LNSE needs the help of adjoint eigenfunctions. An inner-product for two arbitrary vectors $\boldsymbol{a}$ and $\boldsymbol{b}$ is defined as

$(\boldsymbol{a}, \boldsymbol{b}) = \iint_V \boldsymbol{a} \cdot \boldsymbol{b}^{\mathrm{T}} \,\mathrm{d}x\,\mathrm{d}y$, where the superscript T stands for the transpose and V represents the integration region over x–y plane. Based on the inner-product, the adjoint problem of (2.6) can be expressed as

$$(-\mathrm{i}\omega^{\dagger}\boldsymbol{\Gamma}^{\dagger} - \mathscr{L}^{\dagger})\hat{\boldsymbol{p}}^{\dagger} = 0, \tag{2.7}$$

where the superscript † stands for the adjoint variables and operators. It should be noted that boundary terms can be eliminated with proper boundary conditions in the integration by parts. In addition, based on the definition of inner-product, the adjoint and the original problems have the same eigenvalue spectrum.

A bi-orthogonal eigenfunction system $\{\hat{\boldsymbol{p}}_a, \hat{\boldsymbol{p}}_b^{\dagger}\}$ is now formed with the help of eigenfunctions from the original problem $\hat{\boldsymbol{p}}_a$ and the adjoint problem $\hat{\boldsymbol{p}}_b^{\dagger}$. The direct and adjoint equations lead to the following expression:

$$\left((-\mathrm{i}\omega_a\boldsymbol{\Gamma} - \mathscr{L})\,\hat{\boldsymbol{p}}_a, \hat{\boldsymbol{p}}_b^{\dagger}\right) = \left((-\mathrm{i}\omega_b^{\dagger}\boldsymbol{\Gamma}^{\dagger} - \mathscr{L}^{\dagger})\hat{\boldsymbol{p}}_b^{\dagger}, \hat{\boldsymbol{p}}_a\right) = 0, \tag{2.8}$$

where ω_a stands for the eigenvalue of the original problem and $\omega_b^{\dagger}$ stands for the eigenvalue of the adjoint problem. Based on the definition of the adjoint problem, then

$$\left((-\mathrm{i}\omega_b^{\dagger}\boldsymbol{\Gamma}^{\dagger} - \mathscr{L}^{\dagger})\hat{\boldsymbol{p}}_b^{\dagger}, \hat{\boldsymbol{p}}_a\right) = \left(\hat{\boldsymbol{p}}_b^{\dagger}, (-\mathrm{i}\omega_b^{\dagger}\boldsymbol{\Gamma} - \mathscr{L})\hat{\boldsymbol{p}}_a\right). \tag{2.9}$$

With the above equations (2.8) and (2.9), the following relationship can be achieved:

$$\left(\omega_b^{\dagger} - \omega_a\right)\left(\mathrm{i}\boldsymbol{\Gamma}\hat{\boldsymbol{p}}_a, \hat{\boldsymbol{p}}_b^{\dagger}\right) = 0. \tag{2.10}$$

If $\omega_b^{\dagger} = \omega_a$ and one can further define that

$$\left(\mathrm{i}\boldsymbol{\Gamma}\hat{\boldsymbol{p}}_a, \hat{\boldsymbol{p}}_b^{\dagger}\right) = C_0^a, \tag{2.11}$$

where C_0^a represents a normalization constant for a specific mode a. If $\omega_b^{\dagger} \neq \omega_a$, the eigenfunctions are orthogonal to each other, so

$$\left(\mathrm{i}\boldsymbol{\Gamma}\hat{\boldsymbol{p}}_a, \hat{\boldsymbol{p}}_b^{\dagger}\right) = 0. \tag{2.12}$$

Relations (2.11) and (2.12) form a bi-orthogonality condition in a two/three-dimensional domain. An inverse Laplace transform (2.4) is adopted for the return to physical space. Also, generally, the solution of linear Navier–Stokes equations can be expanded in a combination of continuous and discrete modes as

$$\boldsymbol{p}(t) = \underbrace{\sum_m \boldsymbol{C}_m^d \hat{\boldsymbol{p}}_m \,\mathrm{e}^{-\mathrm{i}\omega_m t}}_{\textit{Discrete modes}} + \underbrace{\sum_n \oint \boldsymbol{C}_n^c(k)\hat{\boldsymbol{p}}_n(k)\,\mathrm{e}^{-\mathrm{i}\omega_n(k)t}\,\mathrm{d}k}_{\textit{Continuous modes}}, \tag{2.13}$$

where m and n represent the indices of discrete modes and continuous branches, respectively; k stands for the integration parameter along continuous branches, $\boldsymbol{C}_m^d$ and $\boldsymbol{C}_n^c$ represent the amplitude of those discrete modes and branches, respectively. With relationships (2.6)–(2.13), for a specific discrete mode m, then

$$\boldsymbol{C}_m^d\,\mathrm{e}^{-\mathrm{i}\omega_m t} = \left(\mathrm{i}\boldsymbol{\Gamma}\boldsymbol{p}_m, \hat{\boldsymbol{p}}_m^{\dagger}\right)/C_0^m. \tag{2.14}$$

A generic external force $\boldsymbol{f}$, representing the source term in the flow field, together with the external disturbances $\boldsymbol{g}$ standing for any surface/free-stream perturbations, can

be added to system (2.2). The amplitudes of these additional perturbations are assumed to be small hence the whole system can still be described by the linear approximation. Thus, the inhomogeneous system can be expressed as

$$\left.\begin{array}{c} \boldsymbol{\Gamma}\dfrac{\partial \boldsymbol{p}}{\partial t} - \mathscr{L}\boldsymbol{p} = \boldsymbol{f}, \\ \text{At solid wall/far-field: } \boldsymbol{p} = \boldsymbol{g}. \end{array}\right\} \tag{2.15}$$

Similar to the previous process, a normal-modes assumption is adopted with respect to the force terms and boundary conditions:

$$\hat{\boldsymbol{f}} = \int_0^\infty \boldsymbol{f}\, \mathrm{e}^{\mathrm{i}\omega t}\, \mathrm{d}t, \quad \hat{\boldsymbol{g}} = \int_0^\infty \boldsymbol{g}\, \mathrm{e}^{\mathrm{i}\omega t}\, \mathrm{d}t. \tag{2.16}$$

The relative system in phase space can also be written as

$$(-\mathrm{i}\omega\boldsymbol{\Gamma} - \mathscr{L})\,\hat{\boldsymbol{p}} = \hat{\boldsymbol{f}}, \tag{2.17}$$

with the inhomogeneous boundary conditions $\hat{\boldsymbol{p}} = \hat{\boldsymbol{g}}$ on boundary lines.

Considering a dot product between an adjoint eigenvector $\hat{\boldsymbol{p}}^\dagger$ and (2.17) for any discrete mode m, with integration over the whole domain, we have

$$\left(\hat{\boldsymbol{p}}^\dagger, (-\mathrm{i}\omega_m\boldsymbol{\Gamma} - \mathscr{L})\,\hat{\boldsymbol{p}}_m\right) = (\hat{\boldsymbol{p}}^\dagger, \hat{\boldsymbol{f}}). \tag{2.18}$$

Based on (2.7), the following adjoint homogeneous equation can be obtained:

$$\left(\hat{\boldsymbol{p}}_m, \left(-\mathrm{i}\omega^\dagger\boldsymbol{\Gamma}^\dagger - \mathscr{L}^\dagger\right)\hat{\boldsymbol{p}}^\dagger\right) = \left(\hat{\boldsymbol{p}}^\dagger, (-\mathrm{i}\omega\boldsymbol{\Gamma} - \mathscr{L})\,\hat{\boldsymbol{p}}_m\right) = 0. \tag{2.19}$$

Substituting (2.19) into (2.18), the following relationship is then derived for a specific discrete mode m:

$$\mathrm{i}\,(\omega - \omega_m)\left(\boldsymbol{\Gamma}\hat{\boldsymbol{p}}_m, \hat{\boldsymbol{p}}^\dagger\right) = \left(\hat{\boldsymbol{f}}, \hat{\boldsymbol{p}}^\dagger\right) - B.C. \tag{2.20}$$

Here $B.C.$ represents concomitant boundary terms due to the inhomogeneous boundary conditions determined by using Green formulas (detailed expression is given in Appendix A). With (2.4), (2.14) and (2.20), the following integral equation is derived for the physical perturbation $\boldsymbol{p}_m$:

$$\begin{aligned} \left(\mathrm{i}\boldsymbol{\Gamma}\boldsymbol{p}_m, \hat{\boldsymbol{p}}^\dagger\right) &= -\frac{1}{2\pi}\oint_{-\infty-\mathrm{i}\infty}^{\infty+\mathrm{i}\infty}\left(\mathrm{i}\boldsymbol{\Gamma}\hat{\boldsymbol{p}}_m, \hat{\boldsymbol{p}}^\dagger\right)\mathrm{e}^{-\mathrm{i}\omega t}\,\mathrm{d}\omega \\ &= -\frac{1}{2\pi}\oint_{-\infty-\mathrm{i}\infty}^{\infty+\mathrm{i}\infty}\frac{\left(\hat{\boldsymbol{f}}, \hat{\boldsymbol{p}}^\dagger\right) - B.C.}{(\omega - \omega_m)}\mathrm{e}^{-\mathrm{i}\omega t}\,\mathrm{d}\omega. \end{aligned} \tag{2.21}$$

By closing the Bromwich integral (2.21) in the complex ω-plane, the integral is obtained as the residue value at the point $\omega = \omega_m$:

$$-\frac{1}{2\pi}\oint_{-\infty-\mathrm{i}\infty}^{\infty+\mathrm{i}\infty}\frac{\left(\hat{\boldsymbol{f}}, \hat{\boldsymbol{p}}^\dagger\right) - B.C.}{(\omega - \omega_m)}\mathrm{e}^{-\mathrm{i}\omega t}\,\mathrm{d}\omega = -\mathrm{i}\left[\left(\hat{\boldsymbol{f}}, \hat{\boldsymbol{p}}^\dagger\right) - B.C.\right]\mathrm{e}^{-\mathrm{i}\omega_m t}. \tag{2.22}$$

The amplitude $\boldsymbol{C}_m^d$ for a specific discrete mode m can be recovered as

$$\left|\boldsymbol{C}_m^d\right| = \left|-\mathrm{i}\left[\left(\hat{\boldsymbol{f}}, \hat{\boldsymbol{p}}_m^\dagger\right) - B.C.\right]/C_0^m\right|. \tag{2.23}$$

For the fact that C_0^m is a constant for a specific discrete mode, the adjoint field represents a scaled Green's function for the receptivity problem. In fact, formula (2.23) is consistent

	Λ (°)	δ^* (m)	Re_∞	Re_s	M_s	β
P1	35.0	2.0150×10^{-4}	2826.27	937.33	1.5081	0.1079
P2	40.0	2.0746×10^{-4}	2909.82	1075.44	1.7948	0.1111
P3	45.0	2.1492×10^{-4}	3014.45	1213.22	2.1188	0.1151
P4	50.0	2.2429×10^{-4}	3145.92	1348.36	2.4922	0.1201
P5	55.0	2.3617×10^{-4}	3312.54	1476.33	2.9313	0.1265
P6	60.0	2.5145×10^{-4}	3526.78	1588.28	3.4585	0.1347
P7	65.0	2.7151×10^{-4}	3808.15	1666.99	4.1039	0.1454
P8	70.0	2.9868×10^{-4}	4189.29	1679.10	4.9055	0.1600

Table 1. Flow parameters of eight cases in the present study.

with those obtained from incompressible flows (Giannetti & Luchini 2007). It can thus be considered as a general form for both incompressible and compressible flow systems.

3. Global stability and receptivity of the leading-edge region

The test model is a two-dimensional parabolic body swept with a sweep angle Λ. The model geometry and computational domain are shown in figure 1. The free-stream Reynolds number Re_∞, the sweep Reynolds number Re_s, the free-stream Mach number M_∞, the sweep Mach number M_s and the recovery temperature T_r are defined as

$$\left.\begin{gathered} Re_\infty = \frac{|V_\infty|\delta^*}{\nu_\infty}, \quad Re_s = \frac{W_\infty \delta^*}{\nu_r}, \quad M_\infty = \frac{|V_\infty|}{c_\infty} = 8.15, \quad M_s = \frac{W_\infty}{c_s}, \\ T_r = T_\infty + \sigma(T_0 - T_\infty), \quad \text{where } \sigma = 1 - (1 - \xi_w)\sin^2\Lambda. \end{gathered}\right\} \tag{3.1}$$

Here, ξ_w is a constant for specific free-stream conditions (M_∞ and Λ) and determined based on the study of Reshotko & Beckwith (1958); $R = 0.1$ m represents the radius of the leading edge; V_∞ stands for the free-stream velocity vectors with U_∞, V_∞ and W_∞ along x, y and z direction, respectively. Here T_∞ of 50.93 K and T_0 stand for the free-stream and stagnation temperature, respectively. The parameters c_∞ and c_s are the speeds of sound before and after the leading shock, ν_r represents the kinematic viscosity at T_r. The viscosity length scale δ^* is defined as $\delta^* = \sqrt{\nu_r R/2U_2}$, where U_2 represents chordwise velocity behind the shock. The Prandtl number Pr of 0.71 and the specific heat ratio γ of 1.4 are set following the ideal gas assumption of air. Table 1 lists the parameters of the chosen cases. Here, M_s is used to define the supersonic and hypersonic configurations as mentioned below, and $T_w = T_r$ is the surface temperature, which is used for all cases. The spanwise wavenumber $\beta = 2\pi\delta^*/\lambda_z^*$ is adopted corresponding to the physical wavelength λ_z^* of 11.7 mm.

Firstly, a high-order shock fitting method (Zhong 1998) is employed to obtain the basic flow fields over the largest domain $R3$ as shown in figure 1. In the shock fitting method, the shock is modelled as a boundary of the computational domain; smooth fields can be achieved for the adjoint calculation without considering shock discontinuities (Giles & Pierce 2001). For all cases, 1201 grid points are used along the wall surface and 201 grid points in the wall-normal direction (at least 51 points are clustered inside the boundary layer). Compared with the previous DNS study (Mack *et al.* 2008) with 255×128 grids, the basic flows are adequately resolved in the present grid resolution. A matrix-based high-order global stability analysis is then performed to solve the direct

and adjoint problems. A Krylov–Shur method (Stewart 2002*a*,*b*), based on PETSc (http://www.mcs.anl.gov/petsc) and SLEPc (http://slepc.upv.es) with shift-and-invert spectral transformation is adopted to recover a eigenvalue window (20–50) of interest. Sparse linear algebra packages, MUMPS (http://mumps.enseeiht.fr) and SuperLU (https://github.com/xiaoyeli/superlu_dist) are applied to undertake the inverse of the matrix during the spectral transformations. A complete review of multi-dimensional and global stability analysis techniques is given in Theofilis (2011). More details of the validations/verifications for the present solvers can be found in Xi *et al.* (2021). A standard sixth-order finite difference scheme is used to discretize both directions. Equally spaced grid points are adopted along the wall surface and the following equation is used to cluster grids at the wall:

$$h = H_s \frac{a(1+\eta)}{b-\eta}, \quad a = \frac{\eta_h}{1-2\eta_h}, \quad b = 1+2a. \tag{3.2a–c}$$

Here, η is the uniform grid in computational domain $[-1, 1]$, H_s stands for the distance between the shock and the wall, h represents the wall-normal grid in the physical domain and η_h, set to 0.025, is a location parameter for clustering control. To achieve a grid-independent solution, the number of discretization points is checked for convergence. A large number of grid points up to 5401×401 are employed to identify the structure of direct and adjoint eigenfunctions with a minimum of 20 points per wavelength in each direction for different sizes of computational domains.

The spectrum of the attachment-line modes for CASE P2 is shown in figure 2(*a*). The branches of attachment-line modes are marked by black filled dots. Similar to the incompressible cases (Lin & Malik 1996; Meneghello *et al.* 2015), symmetric ($S1$, $S2$, ...) and antisymmetric ($A1$, ...) modes alternate from the most unstable to the most stable. The leading symmetric mode $S1$ has the highest growth rate. All the attachment-line modes are travelling in the spanwise direction at a nearly constant phase speed around 0.5. For the high-sweep Mach number case (CASE P8), however, as shown in figure 2(*b*), only one symmetric discrete mode is obtained that is marked with S. Based on the recent study (Xi *et al.* 2021), for large sweep Mach numbers, the attachment-line mode is inviscid in nature, while for lower sweep Mach numbers, the attachment-line instability exhibits the behaviours of viscous Tollmien–Schlichting waves.

The leading attachment-line modes are calculated through three different domains (see figure 1). For all domains, the same leading eigenvalues and consistent eigenfunctions are obtained as shown in figure 3. It indicates that the characteristics of attachment-line modes are not much affected by the computation domain size. From figure 3(*a*), the behaviour of the surface-density perturbations, which are normalized with the values at the attachment line, are of great difference in the downstream region $s/R > 1$ for these two cases. Based on eigenfunctions in figure 3(*b*,*c*), it is seen that the downstream perturbations in CASE P2 are of the cross-flow type while those in CASE P8 are of the second Mack-mode type, as highlighted more clearly in figure 4(*e*) (CASE P2) and figure 4(*f*) (CASE P8).

Figure 4(*a*,*b*) display the structures of direct and adjoint eigenvectors obtained from the largest R3 domain for the leading eigenvalues of CASES P2 and P8, respectively. The structures are visualized with the iso-surfaces of the real part of the direct spanwise velocity $\hat{w}$ and the adjoint spanwise velocity $\hat{w}^\dagger$. For both cases, red/blue colours stand for positive/negative values ($\pm 10^{-6}$) for direct eigenfunctions and blue/white colours represent positive/negative values ($\pm 10^{-3}$) for adjoint eigenfunctions. Figure 4(*a*,*b*) display the typical features for the direct global eigenfunctions exhibitting attachment-line instability near the leading edge, while either cross-flow instability (CASE P2) or second Mack mode (CASE P8) dominate downstream flows. For smaller M_s (CASE P2), from

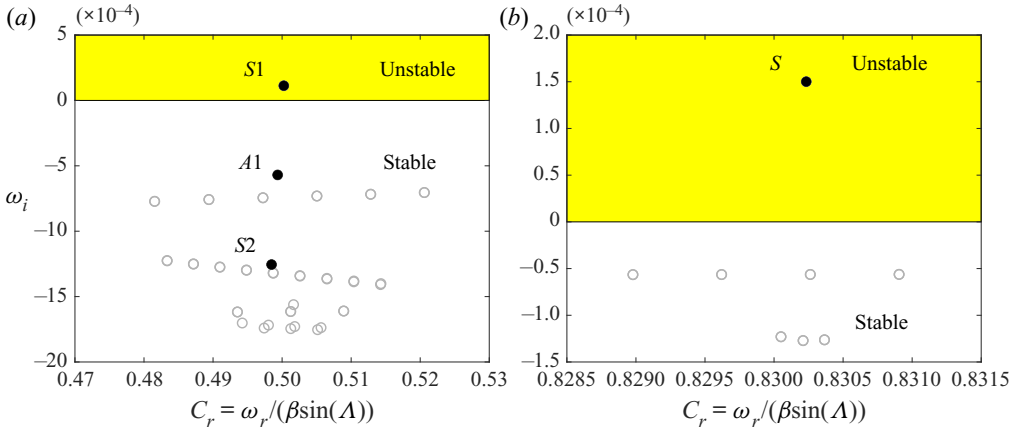

Figure 2. The calculated spectra around the leading attachment-line modes for CASE P2 (*a*) and CASE P8 (*b*) on *R*2 domain. The black, filled dots stand for discrete modes of the attachment-line type and the grey open circles represent eigenvalues from the continuous spectrum or pseudo-spectrum.

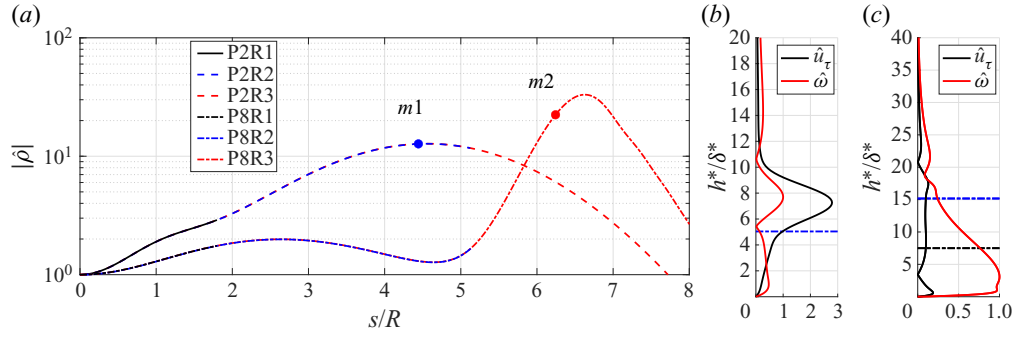

	P2	P8
Small domain (R1)	0.035724347 + 0.00011250136*i*	0.12482622 + 0.00015009545*i*
Mid-sized domain (R2)	0.035724347 + 0.00011250149*i*	0.12482623 + 0.00015009213*i*
Large domain (R3)	0.035724347 + 0.00011250156*i*	0.12482622 + 0.00015009117*i*

Figure 3. (*a*) Dependences of the density perturbations along wall surfaces on different computational domain sizes (R1, R2 and R3 shown in figure 1) for CASES P2 and P8. The leading direct eigenvalues for over different domains are shown in the table. The digits different from the small-domain values are underlined. The two eigenfunctions at *m*1 and *m*2 in panel (*a*) are shown in panels (*b*,*c*). Here, $\hat{u}_\tau$ and h^* stand for chordwise velocity perturbation and dimensional distance away from wall surface, $|\hat{\rho}|$ stands for the norm of density perturbations, and s represents the distance away from the attachment line along the surface. The location of critical layer $c_r = \bar{U}$ and the sonic lines $c_r = \bar{U} + a$ (where $\bar{U}$ represents the spanwise velocity along z direction and a stands for the speed of sound) are indicated by horizontal dash-dotted blue and black lines, respectively.

the attachment-line plane, marked *a*1 in figure 4(*a*) and shown in figure 4(*c*), to the downstream plane, marked *a*2 in figure 4(*a*) and shown in figure 4(*e*), perturbations evolve away from wall surfaces forming cross-flow vortices aligned with external streamlines, as also reported by Mack *et al.* (2008) and Meneghello *et al.* (2015). For larger M_s (CASE P8), despite the similar mode structure at the attachment-line plane, marked *b*1 in figure 4(*b*) and shown in figure 4(*d*), the perturbations at the downstream plane, marked *b*2 in figure 4(*b*) and shown in figure 4(*f*), exhibit the behaviour of the second Mack

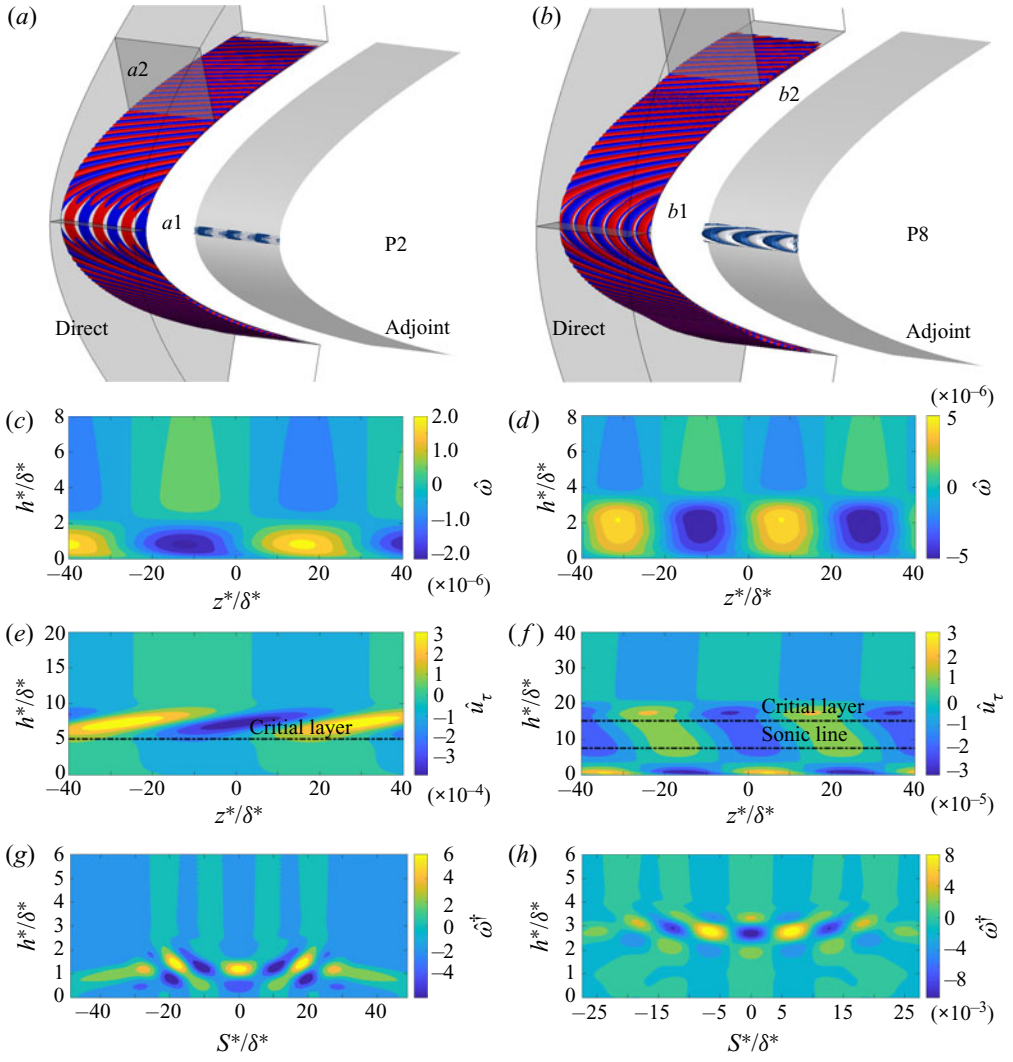

Figure 4. (*a*,*b*) show the direct/adjoint eigenfunctions of the discrete modes for CASE P2 and CASE P8, respectively. (*c*,*d*) show the contours of spanwise velocity $\hat{w}$ of direct eigenfunctions at the attachment-line planes. (*e*,*f*) show the contours of chordwise velocity $\hat{u}_\tau$ of direct eigenfunctions at the further downstream planes. (*g*,*h*) show the contours of spanwise velocity $\hat{w}^\dagger$ of adjoint eigenfunctions at the attachment-line planes. z^* represents the dimensional spanwise location. S^* represents the distance away from the attachment line along the surface, and the positive/negative values distinguish the upper ($y > 0$) and lower part ($y < 0$) of the field.

mode instability with perturbations mainly located below the sonic line. In contrast to the feature that the perturbations of direct mode cover a large area, the adjoint mode appears only in the vicinity of the attachment line as shown in figure 4(*a*,*b*,*g*,*h*). Figure 4(*g*,*h*) show the contours of adjoint spanwise velocity $\hat{w}^\dagger$ for CASE P2 and P8 at the attachment-line planes, respectively. The basic structures of adjoint fields for both cases are similar and the bulk of adjoint fields moves away from the wall surface for large sweep Mach numbers. Moreover, based on the theoretical receptivity analysis on external force $\boldsymbol{f}$, this region is the most responsive to this discrete global mode. In other words, even though the direct global mode covers a large region further away from the attachment line, it is still

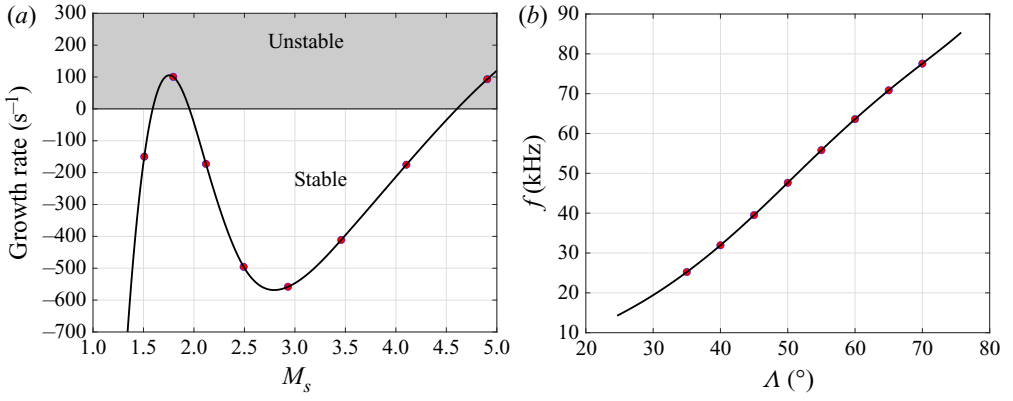

Figure 5. (*a*) Dependence of the growth rates on sweep Mach numbers. (*b*) Dependence of the frequency on sweep angle Λ. The marked red points represent CASES P1–P8.

possible to control/excite the mode by introducing forces at a relatively small region close to the attachment line. This finding is consistent with those from incompressible flows by Meneghello *et al.* (2015), indicating that the leading-edge control might be effective to the hypersonic flows over swept blunt bodies.

The characteristics of the leading attachment-line mode on sweep angles and the relative sweep Mach numbers are shown in figure 5. As the sweep angle varies from 20° to 70°, the growth rate of the leading attachment-line mode shows a rising and then declining trend, reaching the locally highest point around 40°. When the sweep angle further increases, the growth rate of the leading attachment-line mode exhibits the features of monotonous increase and becomes positive again at large sweep Mach numbers. Moreover, this finding is consistent with two facts: the first is that the plane stagnation flow is known to be linearly stable for three-dimensional perturbations, as can be seen as the limit of zero sweep angle for the present cases; the other is that the attachment-line instability is found to become unstable for large sweep angles (Gaillard, Benard & Alziary de Roquefort 1999).

Based on (2.23), the amplitudes of the modes excited by various boundary perturbations are mainly determined by the concomitant boundary term ($B.C.$). From the expression in Appendix A, it is clearly shown that the receptivity is evaluated from the gradients of adjoint variables and physical perturbations on the boundary. Moreover, this procedure permits the extraction of the receptivity amplitude pertaining to any discrete modes for any type of boundary perturbations at any location. Taking the surface perturbations in CASES P2 and P8, for instance, two types of surface perturbation (detailed expressions can be found in Appendix B) are calculated, as shown in figure 6. It demonstrates that the strong receptive regions of the leading attachment-line modes to surface perturbations are in the vicinity of attachment line and the surface perturbations at the exact attachment line are the most effective. Also, the surface vibrations are found to be a little more effective than suction/blowing, because of the higher excited amplitudes. Moreover, as the delta-function form perturbations are used and the basis for representation of LNSE cover the whole domain, the distributed surface perturbations receptivity analyses can be easily performed by integrations along the finite length. Further, as the present framework is from the basis of LNSE, the receptivity problem for the excitation of discrete modes of free-stream disturbances with surface inhomogeneities can be also taken into account.

As mentioned by Tumin (2020), the eigenfunction expansion methods for the two- and three-dimensional problems are the natural extensions of the widely used local cases.

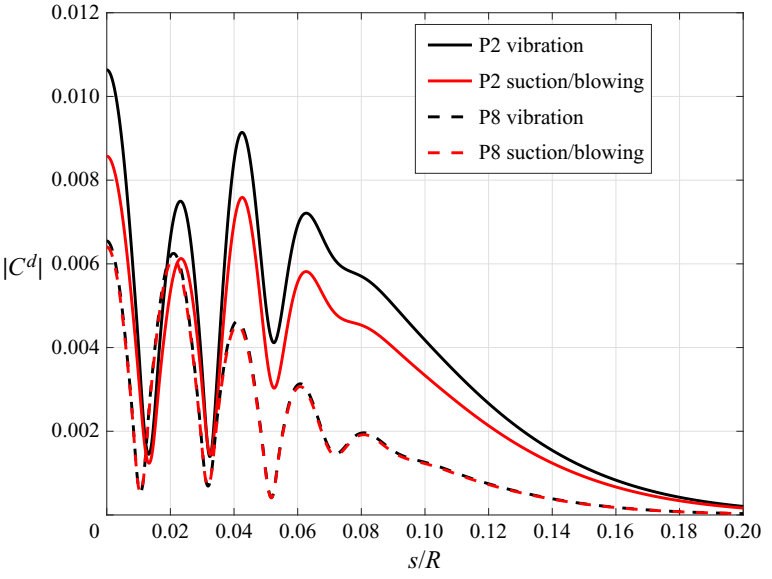

Figure 6. Amplitudes of the leading attachment-line modes excited at different location s/R for surface vibration and suction/blowing. All the eigenfunctions are normalized so that the density components on the wall surface are equal to one at the attachment line.

The analysis of discrete modes is similar for both local and global cases and can be easily performed. However, problems become more complicated with the continuous spectra since the mathematical properties of ordinary and partial differential operators are very different. Although uncertainties associated with the continuous spectra for global cases still exist, the bi-orthogonal eigenfunction system is still a powerful tool for solving global receptivity problems of discrete modes for complex high-speed boundary layers.

4. Conclusions

Global instabilities and receptivities around the leading edge of a swept blunt body are studied in the hypersonic-flow region. The characteristics of the leading attachment-line mode under the variation of sweep angles from 20° to 70° are obtained for the first time. As the sweep angle increases, the growth rates of the leading attachment-line modes exhibit a rising then declining trend and then rising again in which the modes also show the transformation from the features of the cross-flow instability to the second Mack-mode instability further downstream. Moreover, a general bi-orthogonal eigenfunction system for the hypersonic global stability system is established to address receptivity problems to any external forces and boundary perturbations. The receptivity analyses indicate that the leading attachment-line mode is the most responsive to external disturbances in the vicinity of the leading edge, in the hypersonic region. Furthermore, it illustrates that the present framework can be easily applied to both local and non-local linear stability/receptivity analyses for real geometry.

Supplementary material. Supplementary material is available at https://doi.org/10.1017/jfm.2021.217.

Acknowledgements. We appreciate Dr M. Choudhari and Professor A. Hanifi for helpful discussion on the receptivity analysis.

Funding. This work received support from the National Key Project GJXM92579, the National Sci. & Tech. Major Project (2017-II-0004-0016), NSFC Grant 12072173 and the National Key Research and Development Plan through project No. 2019YFA0405201.

Declaration of interests. The authors report no conflict of interest.

Author ORCIDs.
Youcheng Xi https://orcid.org/0000-0002-6484-0231;
Jie Ren https://orcid.org/0000-0001-8448-4361;
Song Fu https://orcid.org/0000-0003-2052-7435.

Appendix A. Concomitant boundary terms

The concomitant boundary terms are determined by using Green formulas. Details for derivation of these terms can be found in supplementary material available at https://doi.org/10.1017/jfm.2021.217. Taking the detailed explicit forms of the operators $\mathscr{L}$, the $B.C.$ term can be expressed as

$$\begin{aligned} B.C. = &- \int_\Gamma \rho^\dagger \rho \hat{u}_{bc}\,\mathrm{d}y + \int_\Gamma \rho^\dagger \rho \hat{v}_{bc}\,\mathrm{d}x \\ &- \int_\Gamma \left(\frac{4\mu}{3Re}\frac{\partial u^\dagger}{\partial x}\hat{u}_{bc} + \frac{\mu}{Re}\frac{\partial v^\dagger}{\partial x}\hat{v}_{bc} + \frac{\mu}{Re}\frac{\partial w^\dagger}{\partial x}\hat{w}_{bc} + \frac{\mu}{RePr}\frac{\partial T^\dagger}{\partial x}\hat{T}_{bc} \right) \mathrm{d}y \\ &+ \int_\Gamma \left(\frac{\mu}{Re}\frac{\partial u^\dagger}{\partial y}\hat{u}_{bc} + \frac{4\mu}{3Re}\frac{\partial v^\dagger}{\partial y}\hat{v}_{bc} + \frac{\mu}{Re}\frac{\partial w^\dagger}{\partial y}\hat{w}_{bc} + \frac{\mu}{RePr}\frac{\partial T^\dagger}{\partial y}\hat{T}_{bc} \right) \mathrm{d}x \\ &- \frac{1}{2}\int_\Gamma \left[\frac{\mu}{3Re}\frac{\partial v^\dagger}{\partial y}\hat{u}_{bc} + \frac{\mu}{3Re}\frac{\partial u^\dagger}{\partial y}\hat{v}_{bc} \right] \mathrm{d}y + \frac{1}{2}\int_\Gamma \left[\frac{\mu}{3Re}\frac{\partial v^\dagger}{\partial x}\hat{u}_{bc} + \frac{\mu}{3Re}\frac{\partial u^\dagger}{\partial x}\hat{v}_{bc} \right] \mathrm{d}x, \end{aligned} \tag{A1}$$

where the superscript † and subscript bc represent the adjoint variables and variables at the boundary line Γ. The direction of the boundary line Γ is defined to ensure the computation domain is always on the left.

Appendix B. Boundary conditions for surface perturbations

The boundary conditions for perturbations can be expressed as

$$\left(\hat{u}_{bc}, \hat{v}_{bc}, \hat{w}_{bc}, \hat{T}_{bc}\right)^{\mathrm{T}} = H(x, y)\left(\hat{u}'_{bc}, \hat{v}'_{bc}, \hat{w}'_{bc}, \hat{T}'_{bc}\right)^{\mathrm{T}}, \tag{B1}$$

where $H(x, y)$ is the shape function of perturbations and is chosen as the Dirac delta function

$$H(x, y) = \delta(S_s - S_l) \tag{B2}$$

in the present study. Here, S_s stands for the surface distance away from the attachment line, and S_l represents a specific location along the surface, where the perturbations are embedded. When a surface is subject to small vibrations, the boundary conditions with

the frequency ω_r can be specified as

$$\hat{u}'_{bc} = -\frac{\partial u}{\partial \boldsymbol{n}} + \mathrm{i}\omega_r \boldsymbol{n}_x, \quad \hat{v}'_{bc} = -\frac{\partial v}{\partial \boldsymbol{n}} + \mathrm{i}\omega_r \boldsymbol{n}_y, \quad \hat{w}'_{bc} = -\frac{\partial w}{\partial \boldsymbol{n}}, \quad \hat{T}'_{bc} = -\frac{\partial T}{\partial \boldsymbol{n}}, \quad \text{(B3}a\text{–}d\text{)}$$

where $\boldsymbol{n} = (\boldsymbol{n}_x, \boldsymbol{n}_y)$ stands for the surface normal direction. In the circumstance of wall-normal blowing/suction, the boundary conditions are given by

$$\hat{u}'_{bc} = \mathrm{i}\omega_r \boldsymbol{n}_x, \quad \hat{v}'_{bc} = \mathrm{i}\omega_r \boldsymbol{n}_y, \quad \hat{w}'_{bc} = 0, \quad \hat{T}'_{bc} = 0. \quad \text{(B4}a\text{–}d\text{)}$$

References

Bertolotti, F.P. 1999 On the connection between cross-flow vortices and attachment-line instabilities. In *IUTAM Symposium on Laminar-Turbulent Transition, Laminar-Turbulent Transition* (ed. H.F. Fasel & W.S. Saric), pp. 625–630. Springer.

Choudhari, M. 1994 *Theoretical Prediction of Boundary-Layer Receptivity. Fluid Dynamics and Co-located Conferences 1994-2223*. American Institute of Aeronautics and Astronautics.

Fedorov, A.V. & Khokhlov, A.P. 2002 Receptivity of hypersonic boundary layer to wall disturbances. *Theor. Comput. Fluid Dyn.* **15** (4), 231–254.

Gaillard, L., Benard, E. & Alziary de Roquefort, T. 1999 Smooth leading edge transition in hypersonic flow. *Exp. Fluids* **26** (1), 169–176.

Giannetti, F. & Luchini, P. 2007 Structural sensitivity of the first instability of the cylinder wake. *J. Fluid Mech.* **581**, 167–197.

Giles, M.B. & Pierce, N.A. 2001 Analytic adjoint solutions for the quasi-one-dimensional Euler equations. *J. Fluid Mech.* **426**, 327–345.

Hill, D.C. 1995 Adjoint systems and their role in the receptivity problem for boundary-layers. *J. Fluid Mech.* **292**, 183–204.

Lin, R.-S. & Malik, M.R. 1996 On the stability of attachment-line boundary layers. Part 1. The incompressible swept Hiemenz flow. *J. Fluid Mech.* **311**, 239–255.

Mack, C.J., Schmid, P.J. & Sesterhenn, J.L. 2008 Global stability of swept flow around a parabolic body: connecting attachment-line and crossflow modes. *J. Fluid Mech.* **611**, 205–214.

Mack, C.J. & Schmid, P.J. 2011 Global stability of swept flow around a parabolic body: features of the global spectrum. *J. Fluid Mech.* **669**, 375–396.

Meneghello, G., Schmid, P.J. & Huerre, P. 2015 Receptivity and sensitivity of the leading-edge boundary layer of a swept wing. *J. Fluid Mech.* **775**, R1.

Obrist, D. & Schmid, P.J. 2003 On the linear stability of swept attachment-line boundary layer flow. Part 2. Non-modal effects and receptivity. *J. Fluid Mech.* **493**, 31–58.

Reed, H.L. & Saric, W.S. 1989 Stability of three-dimensional boundary layers. *Annu. Rev. Fluid Mech.* **21** (1), 235–284.

Reshotko, E. & Beckwith, I.E. 1958 Compressible laminar boundary layer over a yawed infinite cylinder with heat transfer and arbitrary Prandtl number. *NACA Tech. Rep.* 1379. National Advisory Committee for Aeronautics.

Ruban, A.I. 1984 On the generation of Tollmien–Schlichting waves by sound. *Fluid Dyn.* **19** (5), 709–717.

Saric, W.S., Reed, H.L. & White, E.B. 2003 Stability and transition of three-dimensional boundary layers. *Annu. Rev. Fluid Mech.* **35** (1), 413–440.

Stewart, G. 2002*a* A Krylov–Schur algorithm for large eigenproblems. *SIAM J. Matrix Anal. Applics.* **23** (3), 601–614.

Stewart, G. 2002*b* Addendum to 'Krylov–Schur algorithm for large eigenproblems'. *SIAM J. Matrix Anal. Applics.* **24** (2), 599–601.

Theofilis, V. 1998 On linear and nonlinear instability of the incompressible swept attachment-line boundary layer. *J. Fluid Mech.* **355**, 193–227.

Theofilis, V. 2011 Global linear instability. *Annu. Rev. Fluid Mech.* **43** (1), 319–352.

Tumin, A. 2007 Three-dimensional spatial normal modes in compressible boundary layers. *J. Fluid Mech.* **586**, 295–322.

Tumin, A. 2020 LST and the eigenfunction expansion method for linearized Navier–Stokes equations – a summary. *AIAA Paper* 2020-0105.

XI, Y., REN, J. & FU, S. 2021 Hypersonic attachment-line instabilities with large sweep mach numbers. *J. Fluid Mech.* **915**, A44.

ZHONG, X. 1998 High-order finite-difference schemes for numerical simulation of hypersonic boundary-layer transition. *J. Comput. Phys.* **144** (2), 662–709.